Journal of Materials Processing Tech. 344 (2025) 119026

Contents lists available at ScienceDirect

Journal of Materials Processing Tech.

journal homepage: www.elsevier.com/locate/jmatprotec

Research article

Towards understanding the ultrasonic vibration-assisted diamond cutting of ZnO crystals: Surface integrity and tool wear mechanism

Weihai Huang, Takeshi Hashimoto, Jiwang Yan *

Department of Mechanical Engineering, Faculty of Science and Technology, Keio University, 3-14-1 Hiyoshi, Kohoku-ku, Yokohama 223-8522, Japan

ARTICLE INFO

Keywords:
ZnO crystal
Ultrasonic vibration cutting
Machinability
Tool wear
Lubrication
Micro-structured surface

ABSTRACT

Zinc oxide (ZnO) is a promising material for optics and optoelectronics. However, its machining methods are limited, with polishing being virtually the only available technique, which restricts the fabrication of complex shapes. In this study, for the first time, ultraprecision diamond cutting of single-crystal ZnO was explored. Conventional cutting (CC) and ultrasonic vibration-assisted cutting (UVC) experiments were performed in dry and oil mist lubrication environments. It was found that under dry conditions, both CC and UVC resulted in surface fractures owing to the oxidation-induced chemical tool wear. Using oil mist lubrication significantly reduced tool wear, particularly for UVC. As a result, surface roughness was reduced to 1.9 nm Sa. Cutting in the [11−20] direction was more likely to achieve crack-free surfaces on ZnO than cutting in the [1−100] direction under CC; however, the machinability in cutting in the [1−100] direction was improved by applying UVC. Both CC and UVC processes activated basal and pyramidal slip systems in the subsurface region, accompanied by a high density of dislocations located immediately beneath the surface. UVC further promotes polycrystallization and pyramidal slip activity in the subsurface. A microlens array was fabricated with a surface form error of less than 49 nm peak-to-valley and a surface roughness of less than 2.2 nm Sq by integrating slow tool servo diamond turning with ultrasonic vibration assistance under oil mist lubrication. This study reveals the fundamental cutting characteristics of ZnO, provides guidance for ultraprecision cutting of brittle oxide crystals, and validates a potential solution for fabricating micro-structures on ZnO surfaces.

1. Introduction

Single-crystal zinc oxide (ZnO) has attracted attention in various industries due to its wide direct band gap at room temperature, as well as its high electrical and optical performance. The development of applications, including light-emitting diodes (LEDs) [1], optically pumped lasers [2], and ultraviolet (UV) sensor devices [3], and techniques for growing large-sized ZnO substrates with excellent structural perfection [4], have advanced in parallel in recent decades. Currently, chemo-mechanical polishing (CMP) is the primary method for achieving high-quality flat surfaces on ZnO crystals [5]. To enhance the functionality of components, it is essential to fabricate 3D micro-structures on their surfaces. For example, ZnO microlens arrays show great promise for hyperspectral imaging applications [6], and they may also contribute to reducing the structural complexity of ultrahigh-frequency ultrasonic transducers [7]. To achieve high-quality and high-accuracy micro-structured surfaces, ultraprecision diamond cutting is considered a promising machining method [8].

ZnO crystal is a member of the II–VI compound semiconductor family, along with zinc sulfide (ZnS) and zinc selenide (ZnSe) crystals. While extensive research has explored the diamond cutting of ZnS [9] and ZnSe [10], the machining behavior of ZnO is expected to differ. This is primarily due to its unique hexagonal crystal structure, in contrast to the cubic structures of ZnS and ZnSe [11]. On the other hand, although machining studies have been conducted on other hexagonal crystals, such as gallium nitride (GaN) [12] and silicon carbide (SiC) [13] crystals, ZnO's considerably lower hardness (~4.5 GPa) compared to GaN (~18.5 GPa) and SiC (~36 GPa) suggests that its machining characteristics could be different. Moreover, unlike the other crystals mentioned above, the presence of oxygen in ZnO may lead to chemical interactions with diamond cutting tools under high temperatures and pressures, potentially accelerating tool wear [14]. However, to date, no literature is available on the diamond cutting of ZnO, and its machinability remains unclear (Fig. 1).

Ultrasonic vibration-assisted cutting (UVC), which enables high-frequency intermittent contact between the tool and the workpiece, is

* Corresponding author.
E-mail address: yan@mech.keio.ac.jp (J. Yan).

https://doi.org/10.1016/j.jmatprotec.2025.119026
Received 9 July 2025; Received in revised form 7 August 2025; Accepted 9 August 2025
Available online 11 August 2025

Fig. 1. Schematic summarizing the unique properties of ZnO and highlighting the research gaps compared with previous studies. The surface and subsurface damage formation mechanisms and tool wear mechanisms in diamond cutting of ZnO have not yet been revealed.

a well-developed technique for machining difficult-to-cut materials [15]. The prototype is a linear vibration device operating at 40 kHz in the cutting direction, designed for cutting steel using diamond tools [16]. Later on, elliptical vibration cutting, in which two-directional vibrations are applied along the cutting direction and the chip flow direction, was developed [17]. Its demonstrated superiority prompted further research into the application of ultrasonic vibration cutting, particularly in enhancing the critical depth for ductile cutting of brittle materials [18,19] and advancing surface structure fabrication techniques [20,21] through vibration trajectory modulation. In recent years, high-frequency linear ultrasonic vibration devices operating at frequencies greater than 100 kHz have been developed [22], with the expectation of further improving machined surface roughness [23].

UVC has been proven effective in reducing diamond tool wear when machining materials that are prone to chemical reactions with the tool substrate [24]. For example, Pan et al. [25] compared the performance of UVC and conventional cutting (CC) in machining tungsten alloy, and found that UVC can effectively reduce oxidation wear and inhibit the graphitization of diamond tools. Liang et al. [26] evaluated the performance of UVC in machining 316 L stainless steel and observed that material adhesion and friction at the tool-workpiece interface were suppressed due to intermittent cutting, thereby reducing tool erosion and wear. Chen et al. [27] applied UVC to machine Zerodur glass ceramics, which resulted in a reduced flank wear land on the diamond tool and enhanced the machinability of large-scale components. Nevertheless, whether UVC also reduces tool wear when machining ZnO remains to be investigated. In addition to its effect on tool life, ultrasonic vibration assistance may also influence the surface integrity of the machined workpiece through high-frequency vibrational impacts [28]. For example, compared with CC, UVC can reduce the crack length penetrating into the silicon [29] and sapphire [30] subsurface, which is attributed to enhanced phase transformation [31] or reduced energy consumption [32]. It can also produce a thinner recrystallization and crystal transition layers in machined high-entropy alloys due to decreased stress accumulation induced by cyclic disconnection [33]. Similarly, the phase transformation region in the machined subsurface of SiC produced by UVC is significantly smaller than that produced by CC [34]. However, how ultrasonic vibration assistance affects surface and subsurface damage of ZnO remains to be clarified.

Lucca et al. [35] investigated the mechanical response of ZnO using nanoindentation. They found a pop-in phenomenon in the loading curve, indicating dislocation nucleation and the initial yield point. Gao et al. [36] performed nanoscratching on ZnO under varying loads and observed that the resulting deformation and material removal mechanisms transitioned from elastic contact to plastic deformation, and finally to brittle fracture with increasing load. Huang and Yan [37] conducted nanoindentation tests on various ZnO planes and found that the (0001) plane exhibits a higher elastic recovery rate than the other planes, which may induce cracking during the unloading process. The above implies that, though ZnO is a highly brittle material, it can undergo plastic deformation under specific conditions.

In this study, to investigate the machining characteristics of ZnO single crystals, ultraprecision diamond cutting experiments were performed with ultrasonic vibration assistance under both dry and oil mist lubrication conditions, and the results were compared with those obtained using the conventional cutting method. A comprehensive investigation was conducted on the surface topography, chip morphology, cutting force, subsurface damage, and tool morphology. The influence of lubrication on machining characteristics was examined and the interfacial material interaction mechanisms were clarified. The geometrical interference between the tool and workpiece occurring during UVC of curved surfaces was discussed. A microlens array was fabricated using slow tool servo diamond turning combined with ultrasonic vibration assistance, demonstrating the feasibility of creating 3D micro-structures on ZnO surfaces through ultraprecision diamond cutting. The study reveals the effects of tool ultrasonic vibration on the evolution of surface integrity and tool wear during diamond cutting of ZnO, and provides a new approach for fabricating surface micro-structures on ZnO and other brittle oxide crystals.

2. Material and methods

2.1. Experimental setup

A ZnO (0001) wafer with dimensions of $5 \times 5 \times 0.5$ mm^3 and surface roughness of 1.1 nm Sa finished by CMP was used as the workpiece. The experiments were performed using an ultraprecision machine tool (Nanoform X, AMETEK Precitech Inc., USA), as shown in Fig. 2a. The position feedback resolution and the programming resolution for the X, Y, and Z axes of the ultraprecision machine tool are 8 picometers and 10 picometers, respectively. The spindle runout is less than 25 nm. UVC was implemented using an ultrasonic assisted tooling systems (UTS2, son-x GmbH, Germany), which operated in a multi-order bending vibration mode [22]. This enabled the tool to vibrate in the cutting direction (along the Y-axis) with a major amplitude (A) of 0.85 μm, accompanied by a minor amplitude (B) of 0.03 μm in the longitudinal direction (along the Z-axis), at a frequency of 101.68 kHz. Eqs. (1) and (2) represent the vibrations in the cutting direction and longitudinal direction, respectively, with a phase difference of 180 degrees between them [26], which makes the tool undergo linear vibration at an inclination angle (θ) of 2° relative to the cutting direction, as shown in Fig. 2b. A time-amplitude plot of the tool vibration and the corresponding tool motion trajectory are provided in the supplementary materials (Fig. S1). A single-crystal diamond tool (nose radius R = 0.9 mm, rake angle 0°, relief angle 8°, edge radius approximately 50 nm) was used.

$$y(t) = A\cos(2\pi ft - \pi) \tag{1}$$

$$z(t) = B\cos(2\pi ft) \tag{2}$$

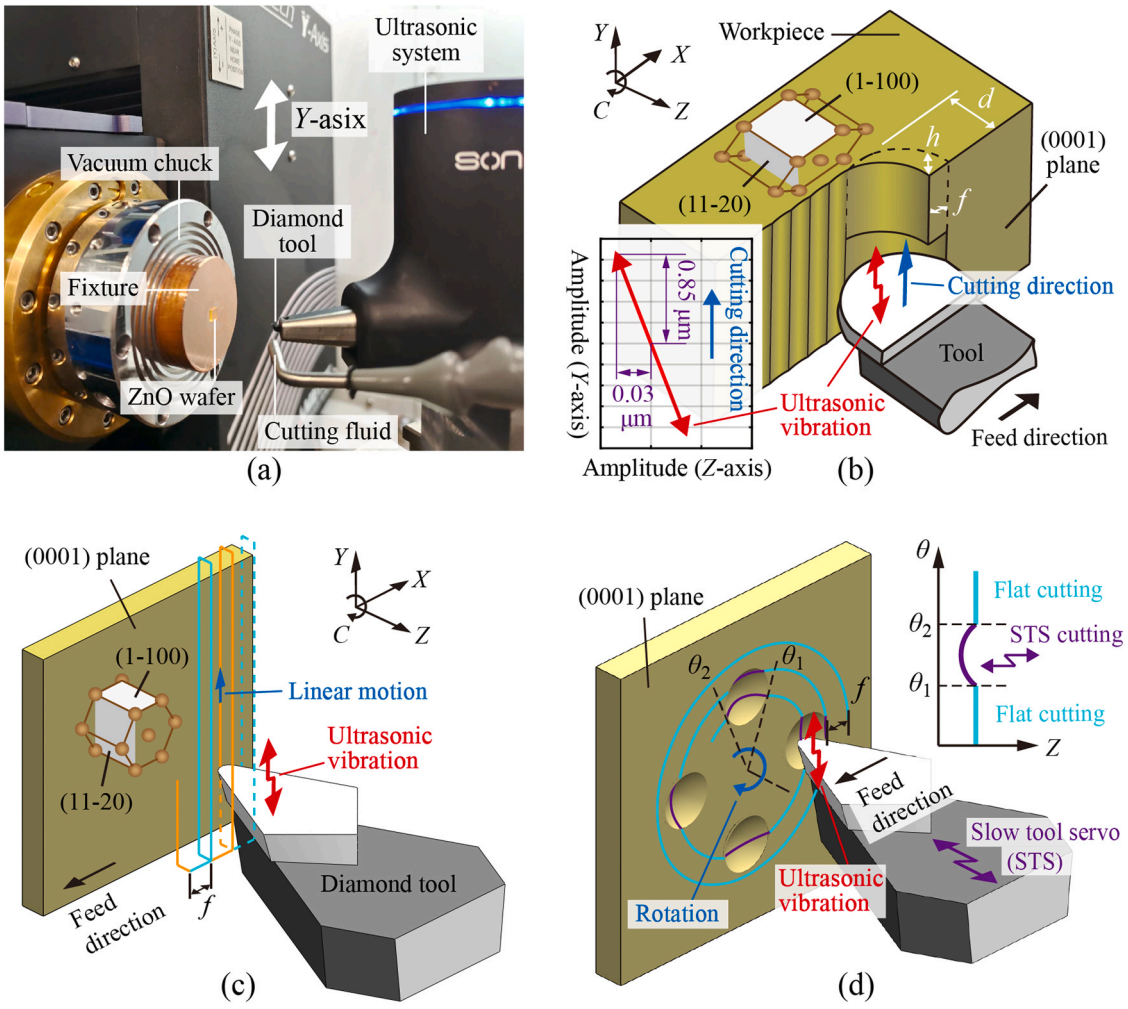

Fig. 2. Experimental setup: (a) experimental equipment photograph; schematic diagrams of (b) ultrasonic vibration-assisted cutting, (c) ruling process, and (d) slow tool servo turning process.

Table 1
Conditions for the ruling and slow tool servo turning processes.

Parameters	Values	
Workpiece	ZnO (0001) plane	
Cutting method	Ruling	Slow tool servo turning
Depth of cut *d*	2 μm	0 – 0.78 μm
Feed *f*	2 μm	1 μm/rev
Cutting speed	500 mm/min	0 – 22 mm/min
Spindle rotation speed	N/A	10 rpm
Cutting direction	[1−100] and [11−20]	All directions
Lubrication conditions	Dry and oil mist	Oil mist
Ultrasonic vibration assistance	ON and OFF	ON

2.2. Ruling process

To understand the influence of crystal anisotropy on the machining characteristics, a ruling process was first employed to maintain a constant relationship between the cutting direction and the crystal orientation throughout each cutting cycle, as shown in Fig. 2c. The tool moved back and forth along the *Y*-axis relative to the workpiece. After each cutting pass, a step feed (*f*) was executed in the *X*-axis. Two typical cutting directions [1−100] and [11−20] were selected, which are normal to the *m*-plane (1−100) and *a*-plane (11−20) of ZnO crystals. Switching between these directions was achieved by rotating the workpiece 90° around the *C*-axis. For each cutting direction, both conventional cutting and ultrasonic vibration-assisted cutting were performed under two lubrication conditions: dry and oil mist. The oil mist cutting was conducted at an air pressure of 0.5 MPa and an oil consumption rate of 1.1 g/h (PS-FM-A, Palace Chemical Co., Ltd.). The cutting speed was set to 500 mm/min, and the depth of cut *d* was set to 2 μm. The tool step feed was set to 2 μm, resulting in a maximum undeformed chip thickness of 131 nm, calculated according to the ductile-regime cutting model [38]. The cutting parameters are summarized in Table 1. A piezoelectric dynamometer (Kistler 9256C2) was used to measure the cutting forces with a sampling frequency of 5 kHz. The sensitivity of the dynamometer in the *X*, *Y*, and *Z* directions is 12.93 pC/N, 25.97 pC/N, and 25.59 pC/N, respectively, with corresponding force resolutions of approximately 0.774 mN, 0.385 mN, and 0.391 mN. In dry cutting, chips were collected for observation. After cutting, scanning electron microscopy (SEM), laser micro-Raman spectroscopy, and cross-sectional transmission electron microscopy (X-TEM) were used to characterize the chips and machined surfaces. The samples for X-TEM observation were prepared by focused ion beam (FIB) milling, and a protective platinum layer was coated on the workpiece prior to the FIB milling.

2.3. Slow tool servo turning process

To validate the potential of ultraprecision diamond cutting for fabricating complex shapes on ZnO, a microlens array was machined using a slow tool servo turning process combined with ultrasonic

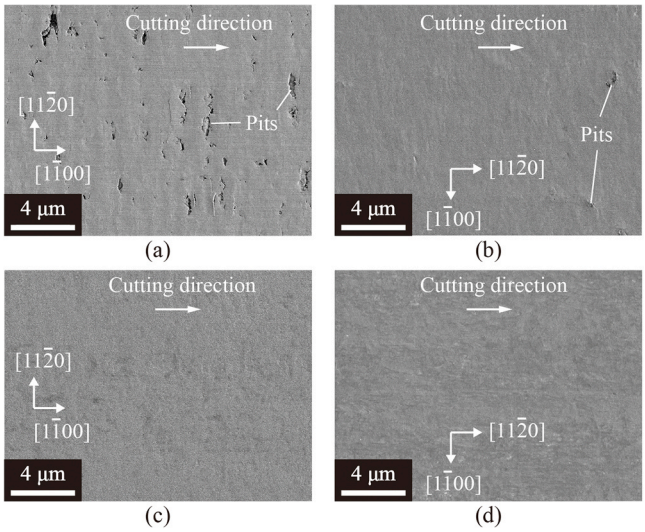

Fig. 3. SEM images of ZnO surfaces machined under dry conditions with unused tool edges: (a) by CC along the [1−100] and (b) [11−20] directions, (c) by UVC along the [1−100] and (d) [11−20] directions. (SEM parameters: accelerating voltage of 1.0 kV, and working distance of 3.0 mm.).

vibration-assisted cutting under oil mist lubrication conditions, as illustrated in Fig. 2d. Four lenses positioned at angular positions $C = 0°$, 90°, 180°, and 270°, with cutting directions alternately aligned with the <1−100> and <11−20> crystal orientations. The X and Y spacings between the lenses were 250 μm. Each lens was designed with a diameter of 125 μm and a curvature radius of 2.5 mm. Consequently, the lenses were fabricated with a depth of cut varying between 0 and 0.78 μm. To ensure improved surface roughness and form accuracy of the lenses, the tool feed rate was set to 1 μm/rev, and the spindle rotation speed was maintained at 10 rpm. The cutting parameters for microlens array fabrication are also listed in Table 1. After cutting, the surface roughness and form error of the machined lenses were measured using a white light interferometer. To analyse the form error, spherical form removal with a curvature radius of 2.5 mm (matching the design specification) was applied to each lens surface. The resulting deviation from the ideal design represents the form error. Surface roughness was then extracted by further applying a Gaussian filter to the form error map, with a cut-off wavelength of 25 μm, in accordance with ISO standards [39].

3. Results and discussion

3.1. Surface topography

Fig. 3 shows the ZnO surfaces machined under dry conditions with unused tool edges. During CC, many pits formed when cutting along the [1−100] direction, as shown in Fig. 3a. These pits were short (submicron scale) in the cutting direction and elongated (micron scale) perpendicular to it, resulting from cracks propagating preferentially along the [11−20] direction. In contrast, fewer pits were observed when cutting along the [11−20] direction, with the length of the pits perpendicular to the cutting direction being notably reduced, as shown in Fig. 3b. These results indicate that cutting along the [11−20] direction is more effective for producing high-quality surfaces than cutting along the [1−100] direction. This could be attributed to the tensile stress, which serves as the driving force for crack initiation and is primarily exerted normal to the (11−20) and (1−100) planes when cutting along the [11−20] and [1−100] directions, respectively. Moreover, the atomic packing density and bond strength are slightly higher on the (11−20) plane than on the (1−100) plane. This is consistent with the nanoindentation results on the ZnO (0001) plane, where the extent of

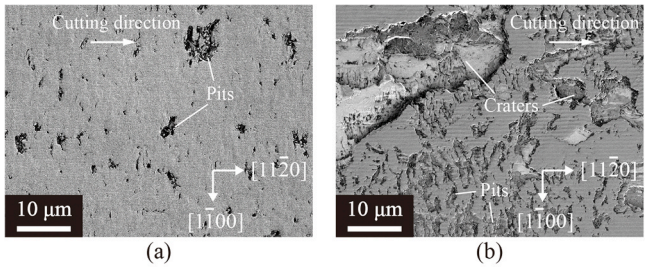

Fig. 4. SEM images of ZnO surfaces machined under dry conditions along the [11−20] direction after cutting ~8 m: (a) by CC, and (b) by UVC. (SEM parameters: accelerating voltage of 1.0 kV, and working distance of 3.0 mm.).

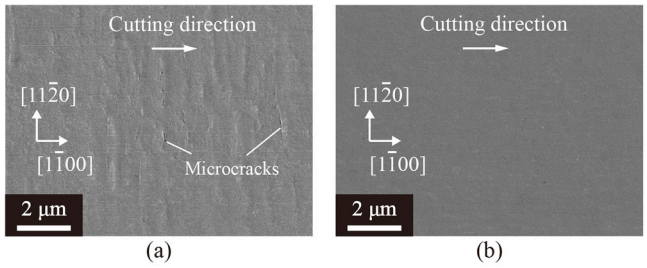

Fig. 5. SEM images of surfaces machined in oil mist lubrication conditions along the [1−100] direction after cutting ~8 m: (a) by CC, and (b) by UVC. (SEM parameters: accelerating voltage of 1.0 kV, and working distance of 3.0 mm.).

cracks along the residual indent edges was smaller when the edges were aligned parallel to the (11−20) plane than to the (1−100) plane [37]. During UVC, however, a smooth surface was obtained regardless of whether the cutting direction is along the [1−100] or [11−20] direction, as shown in Fig. 3c,d, with surface roughness values of 3.5 nm Sa and 3.1 nm Sa, respectively, measured over an area of 170 μm^2 (Fig. S2). This suggests that the machinability of ZnO during the cutting process can be significantly enhanced by applying ultrasonic vibration to the tool, as will be further discussed in Section 3.5.

However, after cutting for a distance of approximately 8 m under dry conditions, the quality of the machined surface deteriorated in both the CC and UVC processes, as presented in Fig. 4, even though these surfaces were obtained by cutting along the [11−20] direction, which had previously been identified in Fig. 3 as more prone to achieving a crack-free surface. For the surface machined by CC, as illustrated in Fig. 4a, both the size and number of pits were greater than those observed in Fig. 3b. Fine tool marks in the cutting direction also became more noticeable on the machined surface. In contrast, the surface machined by UVC, as shown in Fig. 4b, exhibited even poorer quality than that of the surface machined by CC. Numerous micron-scale pits, along with some large craters tens of microns in size, were formed on the surface. Deep and wide tool marks were also formed in the cutting direction, with the distance between adjacent marks smaller than the tool feed pitch. These results suggest that the tool underwent significant and rapid wear during the cutting of the ZnO crystal under dry conditions. The tool wear observations will be detailed in Section 3.6.

On the other hand, another unused tool was employed for the machining of ZnO under oil mist lubrication. Smooth surfaces were obtained under both CC and UVC, as shown in Fig. 5, even though the cutting edges had already been used to cut a length of approximately 8 m (a similar cutting distance as in Fig. 4), and the cutting direction was along the [1−100], which exhibited poor machinability under dry conditions as shown in Fig. 3. For the surface machined by CC, as shown in Fig. 5a, numerous fine microcracks were distributed perpendicular to the cutting direction across the surface; however, they did not result in pit formation. In contrast, the surface machined by UVC, as shown in

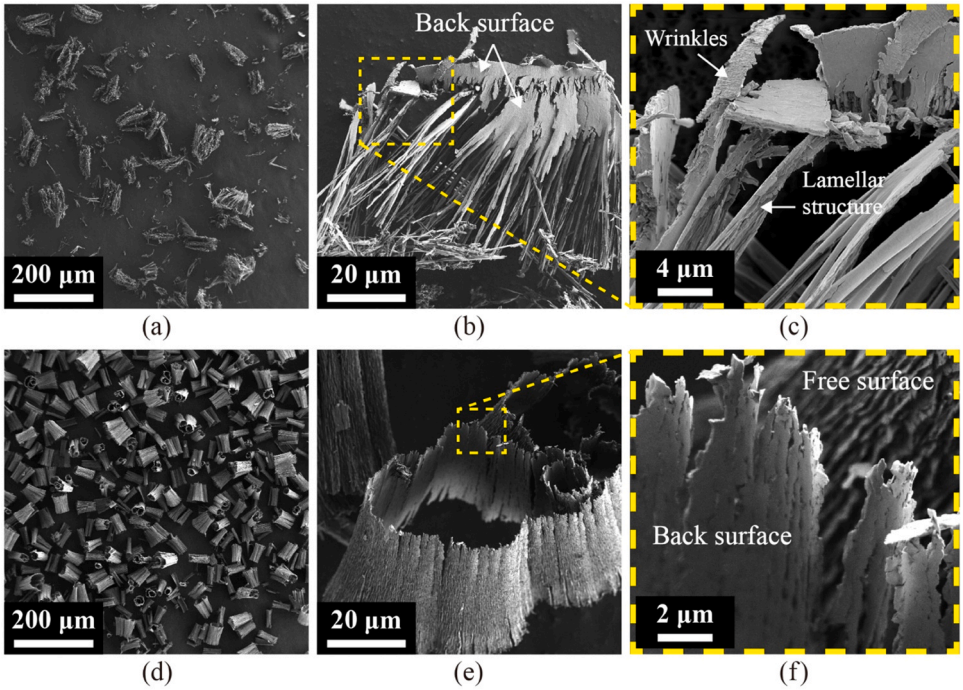

Fig. 6. SEM images of cutting chips generated under dry conditions along the [11−20] direction with unused tool edges: (a) overall chip shape, (b) close-up view of a representative chip, and (c) high-magnification view of the chip structure formed using CC; (d–f) corresponding UVC-processed chips under identical conditions. (SEM parameters: accelerating voltage of 1.0 kV, and working distance of 3.0 mm.).

Fig. 5b, exhibited an extremely smooth morphology without any microcracks, and the surface roughness was reduced to 1.9 nm Sa (Fig. S3). These results indicate that oil mist lubrication is conducive to achieving high-quality surfaces on ZnO. Moreover, the application of ultrasonic vibration further enhances the beneficial effects of oil mist lubrication. It is noted that the current cutting parameters ($f = 2$ μm, $d =$ 2 μm), corresponding to a maximum undeformed chip thickness of 131 nm, represent the boundary between CC and UVC. To achieve a completely crack-free surface under CC, the feed rate or depth of cut needs to be reduced. In contrast, using UVC, a crack-free surface may still be obtained even when these parameters are increased. Therefore, the critical cutting parameters required to achieve high-quality surfaces

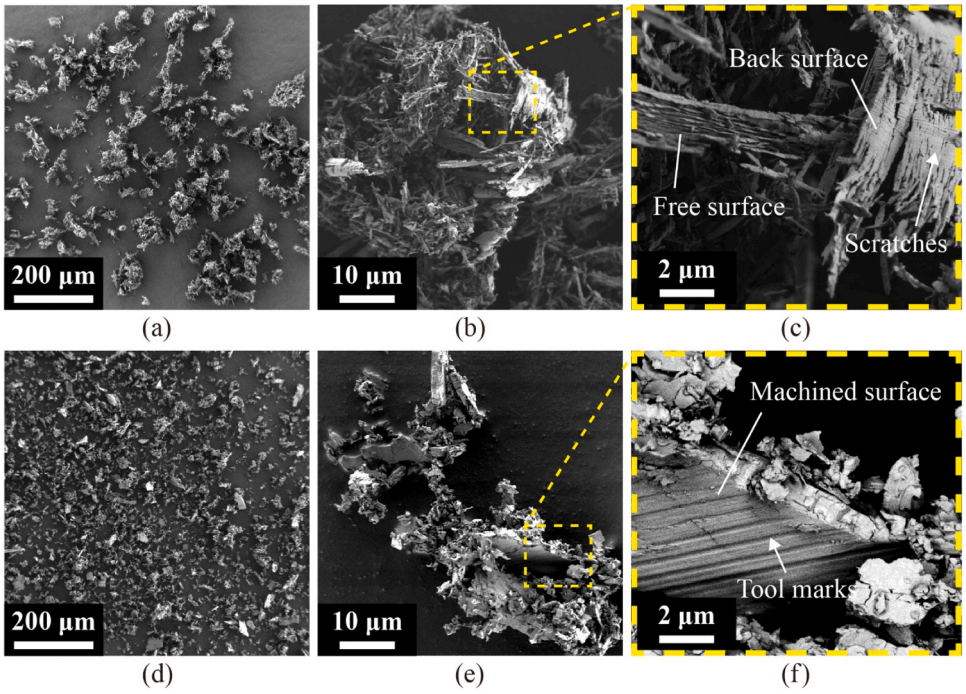

Fig. 7. SEM images of cutting chips generated under dry conditions along the [11−20] direction after cutting ~8 m: (a) overall chip shape, (b) close-up view of a representative chip, and (c) high-magnification view of the chip structure formed using CC; (d–f) corresponding UVC-processed chips under identical conditions. (SEM parameters: accelerating voltage of 1.0 kV, and working distance of 3.0 mm.).

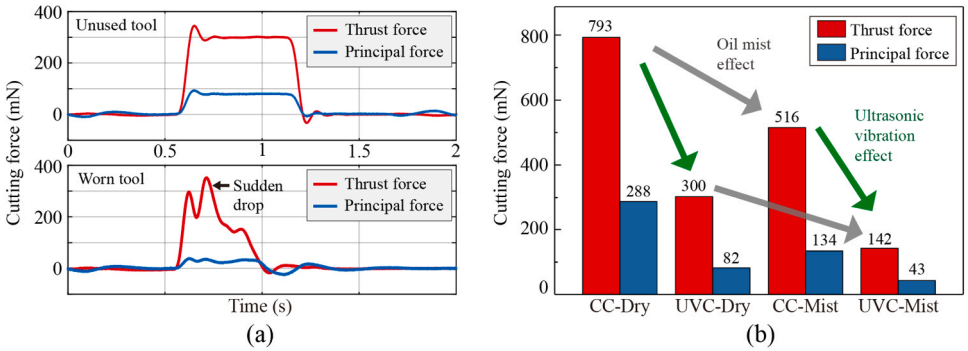

Fig. 8. Cutting forces analysis: (a) typical dynamic force curves during dry cutting under different tool conditions with UVC assistance, (b) comparison of cutting forces obtained during stable cutting under various cutting conditions.

under both CC and UVC need to be investigated in future work. It is also worth noting that the tool vibration-induced fine periodic marks along the cutting direction, which are commonly observed in the cutting of steel [26] or high-entropy alloys [40], were not observed on the ZnO surface (Fig. S4). This may be attributed to the low cutting speed (0.5 m/min) and the small longitudinal vibration amplitude (0.03 μm), which result in a very small theoretical vibration mark height. Furthermore, unlike metals with excellent plasticity, ZnO does not allow the tool trajectory to be effectively transferred to the machined surface.

3.2. Chip morphology

To further understand the material removal behaviour during CC and UVC processes, the morphology of the cutting chips generated while cutting along the [11−20] direction under dry conditions was characterised. During CC with an unused cutting edge, the chips were generally characterized by a discontinuous, curly shape, as shown in Fig. 6a. A close examination of a typical chip (Fig. 6b) revealed that the upper part of the chips appeared intact, while the lower part branched out as curling needles. The back surface of the entire chip, i.e., the side that contacted the tool, was smooth. Upon further magnification, the free surface of the chip, i.e., the side exposed and not in contact with the tool, exhibited distinct features: the upper part showed very dense wrinkles, while the lower part displayed a sparse lamellar structure, as shown in Fig. 6c. These observations suggest that, from the upper to lower parts, the chips formed by extrusion (around the tool tip) transitioning to shear deformation (around the uncut shoulder). In contrast, during UVC, the generated chips exhibited a continuous ribbon-like shape, as shown in Fig. 6d. In the close-up views (Fig. 6e,f), the chip width and thickness appeared uniform. The back surface was smooth, while the free surface displayed a lamellar structure. These characteristics indicate that the chip was formed through stable shear deformation, which contributes to the formation of a smooth machined surface.

The cutting chips generated by the tool after a cutting distance of approximately 8 m were also characterized. During CC, the chips generally exhibited a clustered morphology, agglomerated from numerous disordered thin fragments, as shown in Fig. 7a,b. Upon magnification, lamellar structures were observed on the free surfaces of the fragments, while scratches were visible on their back surfaces, as shown in Fig. 7c, indicating that the chips were formed through a shearing mechanism and the tool edge was worn. In contrast, during UVC, fine irregular block-shaped chips were formed, as shown in Fig. 7d. These blocks were observed to be thick and surrounded by numerous particles but lacked evident lamellar or layered structures, as shown in Fig. 7e, indicating that the material removal likely occurred through a brittle fracture mechanism rather than plastic shearing [41]. Fig. 7f presents an enlarged view of a large block, one side of which featured a flat surface with tool marks, indicating that the chip was peeled off from the machined surface through lateral cracking. This observation helps to explain the formation of surface craters on the machined surface shown in Fig. 4b. It is worth noting that the tool marks observed on the machined surface were not caused by the tool feed, because, under the present cutting parameters, the theoretical residual height between tool passes is too small (<1 nm), such that feed marks typical of conventional metal cutting cannot be observed. Instead, these marks resulted from the replication of the worn tool edge, which exhibited multiple micro-chippings (will be discussed in Section 3.6), onto the machined surface.

3.3. Cutting force

The cutting forces during the ruling experiments conducted under various conditions, i.e., CC and UVC with either dry or oil mist lubrication, were measured. As shown in Fig. 2c, since the tool stops after each cutting pass and returns to the starting point for the next cut, vibrations are generated during the reverse motion, causing fluctuations in the cutting force (Fig. S5). The dynamic force curves for one of the ruling passes during UVC under dry conditions are presented in Fig. 8a. At the beginning of the ruling process, the unused tool produced stable cutting forces, remaining nearly constant throughout most of the cutting process, except during the initial tool-workpiece engagement phase, as shown in the upper part of Fig. 8a. The force result is in accordance with the formation of a smooth machined surface (Fig. 3d). However, in the cutting force curve obtained using the worn tool, sudden drops in thrust force can be observed, as shown in the lower part of Fig. 8a. This may be attributed to material fracture on the machined surface, caused by partial loss of contact between the tool flank face and the workpiece, as evidenced by the severe brittle fracture observed on the machined surface (Fig. 4b), likely resulting from tool edge wear. To evaluate the cutting performance within the effective cutting distance, the stable cutting forces measured in the early stage of the ruling process under various cutting conditions were compared, as shown in Fig. 8b. In all cases, the thrust force was significantly greater than the principal force. With other factors remaining constant, the forces in UVC were lower than those in CC. In addition, the forces under oil mist lubrication were lower than those under dry conditions. Consequently, UVC with oil mist lubrication produced the minimum cutting forces. There may be two reasons for the force reduction measured during UVC. One is that the dynamometer's sampling frequency was lower than the tool vibration frequency, thus the obtained values in UVC represent average cutting forces [26,40]. The other is that vibration enhanced the lubrication effect by forming a lubricating film between the tool and the workpiece via the vibration-induced intermittent tool-workpiece contact.

3.4. Raman spectroscopy

The Raman spectra of the ZnO surfaces machined by CC and UVC, as well as the cutting chips generated during these processes, are examined

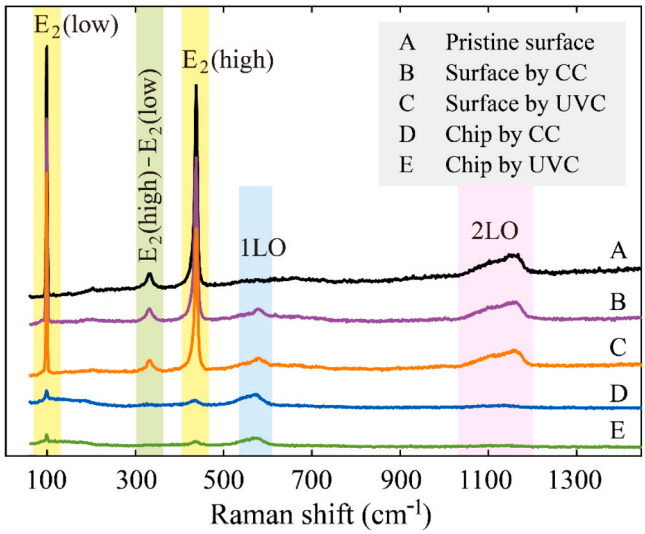

Fig. 9. Comparison of ZnO Raman spectra between the pristine surface, machined surfaces, and collected chips.

and presented in Fig. 9. A spectrum obtained from the pristine surface was also provided for comparison. For the spectrum of the pristine surface, two strong Raman peaks at 99 cm^{-1} and 437 cm^{-1} corresponding to the E_2(low) and E_2(high) modes were observed, which are attributed to the sublattice vibrations of zinc and oxygen, respectively [42]. In addition, two weak peaks were detected near 333 cm^{-1} and 1160 cm^{-1}, representing the E_2(high)−E_2(low) mode and second-order 2LO mode [43]. However, for the machined surfaces produced by both CC and UVC, a new broad peak near 578 cm^{-1} was observed, corresponding to the overlap of the A_1(LO) and E_1(LO) modes, which is assigned collectively to the 1LO mode. This suggests that the cutting process induced defects in machined ZnO, including lattice disorder and oxygen vacancies [42,44]. For the spectra of the cutting chips, the intensities of the E_2(low) and E_2(high) peaks were significantly decreased compared to those of the pristine and machined surfaces, while the 1LO peak maintained a similar intensity to that observed on the machined surfaces, indicating a deterioration in the crystalline quality of the wurtzite-structured ZnO [45]. The Raman spectra of the chips are akin to those of the rock salt phase of ZnO, which is transformed from the wurtzite phase under a pressure higher than 9 GPa [46]. It should be noted that the phase transformation observed in the UVC process is induced by the instantaneous cutting force at the moment of tool–workpiece contact, which, according to simulation studies [47], is believed to be equivalent to that in conventional cutting, rather than by the measured average cutting force.

3.5. Subsurface microstructure

Since dry cutting along the [1−100] direction by CC caused more severe surface damage, while UVC significantly improved the surface quality, the subsurface microstructure of the workpiece machined by both CC and UVC under these conditions has been analysed and discussed. Two TEM samples were taken from surfaces machined along the [1−100] direction under CC and UVC, respectively. The cross-sectional plane of each sample is parallel to the cutting direction. Fig. 10 shows the TEM observation results of the sample taken from the CC-processed surface. Fig. 10a presents an overview of the subsurface damage distribution, in which cracks were observed extending up to approximately 700 nm beneath the surface. Although the crack propagation directions did not exhibit a clearly consistent pattern, they are likely to occur along the {1−101} and (0001) planes. A selected-area electron diffraction

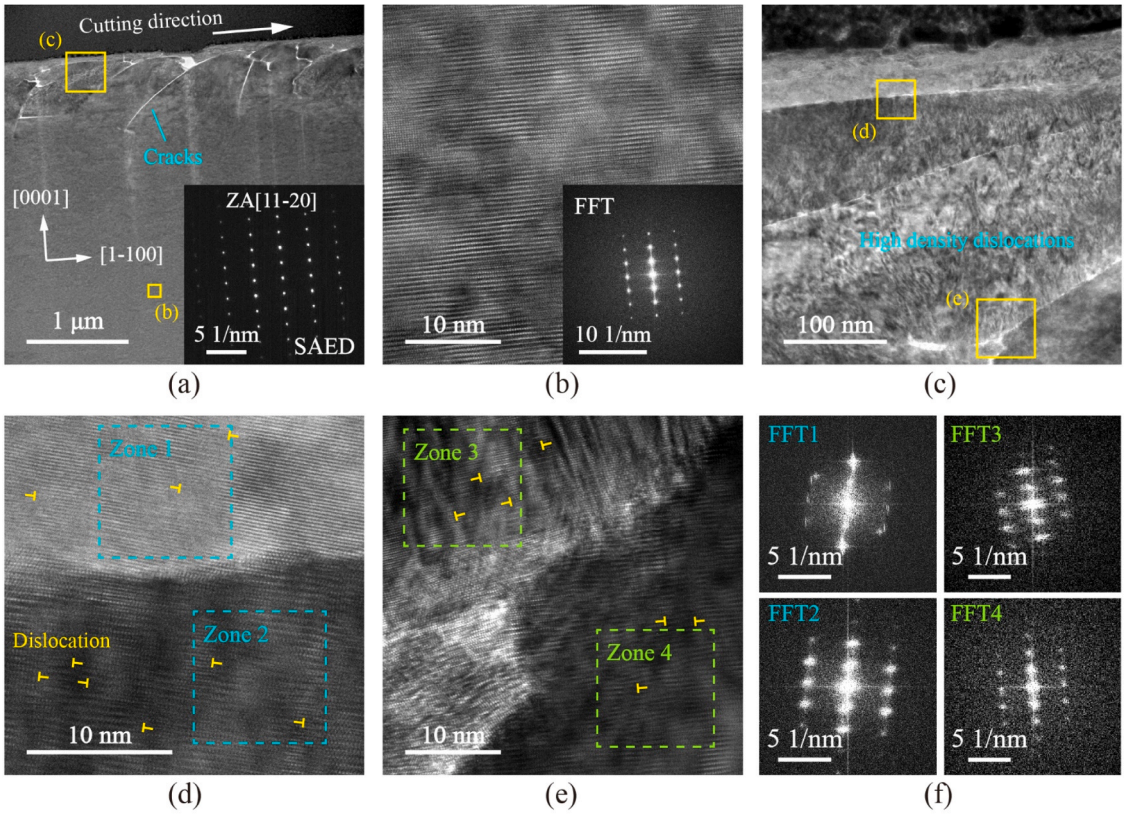

Fig. 10. Cross-sectional TEM images of ZnO subsurface region after CC under dry conditions: (a) overview showing the distribution of subsurface damage; (b) high-resolution image of a region located deep below the surface; (c) magnified view of the subsurface area indicated in (a); (d, e) high-resolution images of the areas indicated in (c); (f) Fast Fourier Transforms (FFT) of the regions shown in (d) and (e).

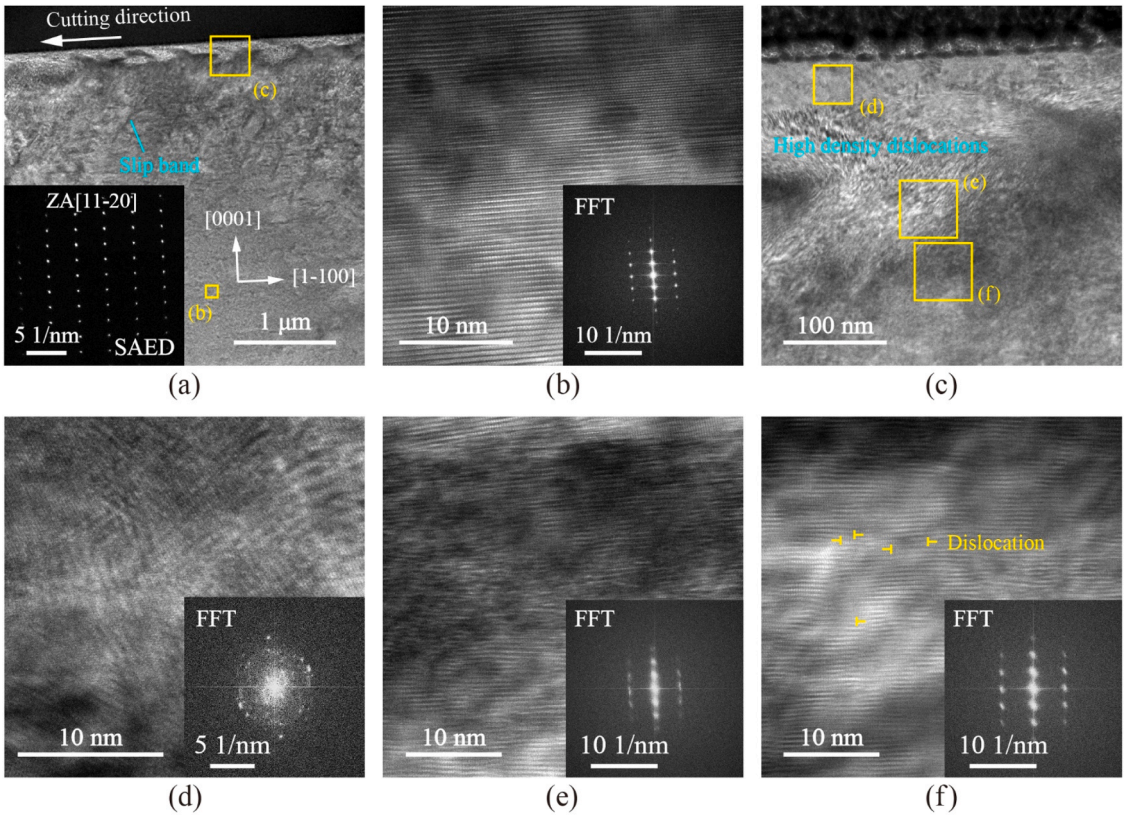

Fig. 11. Cross-sectional TEM images of ZnO subsurface region after UVC under dry conditions: (a) overview showing the distribution of subsurface damage; (b) high-resolution image of a region located deep below the surface; (c) magnified view of the subsurface area indicated in (a); (d–f) high-resolution images of the areas indicated in (c), which are located progressively deeper below the surface.

(SAED) pattern from a region deep below the surface, obtained using an aperture size of 1 μm, is displayed in the inset. The patterns exhibit sharp and well-defined diffraction spots, indicating high crystallinity, and can be used as a reference for evaluating the extent of subsurface damage in other regions. A high-resolution image of a region located deep below the surface is provided in Fig. 10b. The uniform lattice spacing with no obvious distortion indicates that the deep subsurface is free from machining-induced damage, and its fast Fourier transform (FFT) pattern also agrees with the SAED pattern in Fig. 10a. Upon magnifying the near-surface region, as shown in Fig. 10c, a high density of dislocations was observed (Fig. S6), and ultrafine cracks were observed to pass through these dislocation-rich regions, segmenting them into several layers. In particular, the layer closest to the surface was formed by an ultrafine crack that propagated parallel to the surface at a depth of approximately 50 nm. Fig. 10d presents a high-resolution TEM image of the region surrounding this surface-parallel crack, with FFT analyses conducted in the regions above and below it, as shown in Fig. 10f. The FFT pattern of the upper region (zone 1) exhibited blurry spots, whereas that of the lower region (zone 2) displayed much clearer diffraction spots, indicating that high levels of strain and dislocations had occurred in the region closest to the surface. Moreover, these FFT patterns were structurally identical to the SAED pattern but were rotated at different angles, which could be attributed to lattice misorientation caused by crack formation between the near-surface material and the pristine substrate. Fig. 10e presents a high-resolution TEM image of the area surrounding another ultrafine crack at a depth of approximately 300 nm, and the FFT analysis of the regions above and below the crack is shown in Fig. 10f. The FFT pattern of the lower region (zone 4) was sharper than that of the upper region (zone 3), indicating that strain and dislocations had been reduced (Fig. S6), possibly due to the formation of cracks relaxing the strain energy. Moreover, their lattice misorientation relative to the pristine substrate was significantly suppressed, as evidenced by FFT patterns exhibiting alignment with the SAED pattern. It is also worth noting in Fig. 10f that, from the area close to the inner substrate (FFT4) to the area near the surface (FFT1), the SAED pattern exhibits a clockwise rotation, indicating that the lattice deflection rotated in the same direction. This lattice rotation is likely caused by friction at the tool flank face, and the direction of cutting is consistent with the direction of the applied force.

Fig. 11 shows TEM observations of the sample taken from the UVC-processed surface. Fig. 11a presents an overview of the subsurface damage distribution, in which no cracks were formed, while slip bands, characterized by long and straight lines, were observed. A SAED pattern from a region deep below the surface, exhibiting regularly arranged diffraction spots, is displayed in the inset and serves as a reference for comparing the extent of subsurface damage in other regions. Fig. 11b shows a high-resolution image of a region located deep below the surface, exhibiting a well-ordered lattice, and its FFT pattern is consistent with the SAED pattern shown in Fig. 11a. Upon magnifying the near-surface region, as shown in Fig. 11c, a high density of dislocations was observed. Subsequently, three high-resolution TEM images were taken from the areas indicated in Fig. 11c, corresponding to regions located progressively deeper below the surface, as shown in Fig. 11d-f. For the region closest to the surface, as shown in Fig. 11d, Moiré fringes were observed. The FFT patterns also exhibited concentric rings surrounding the central spot. These results indicate that UVC induced a high-density network of dislocations in the subsurface region immediately below the machined surface, resulting in the polycrystallization in the ZnO single crystal. For the regions at depths of approximately 150 nm and 200 nm, the lattice fringes became progressively more ordered with increasing depth, and their FFT patterns also appeared sharper, as shown in Fig. 11e,f. In other words, polycrystallization occurred only at the very near surface, while the subsurface region beneath it remained a single-crystal structure.

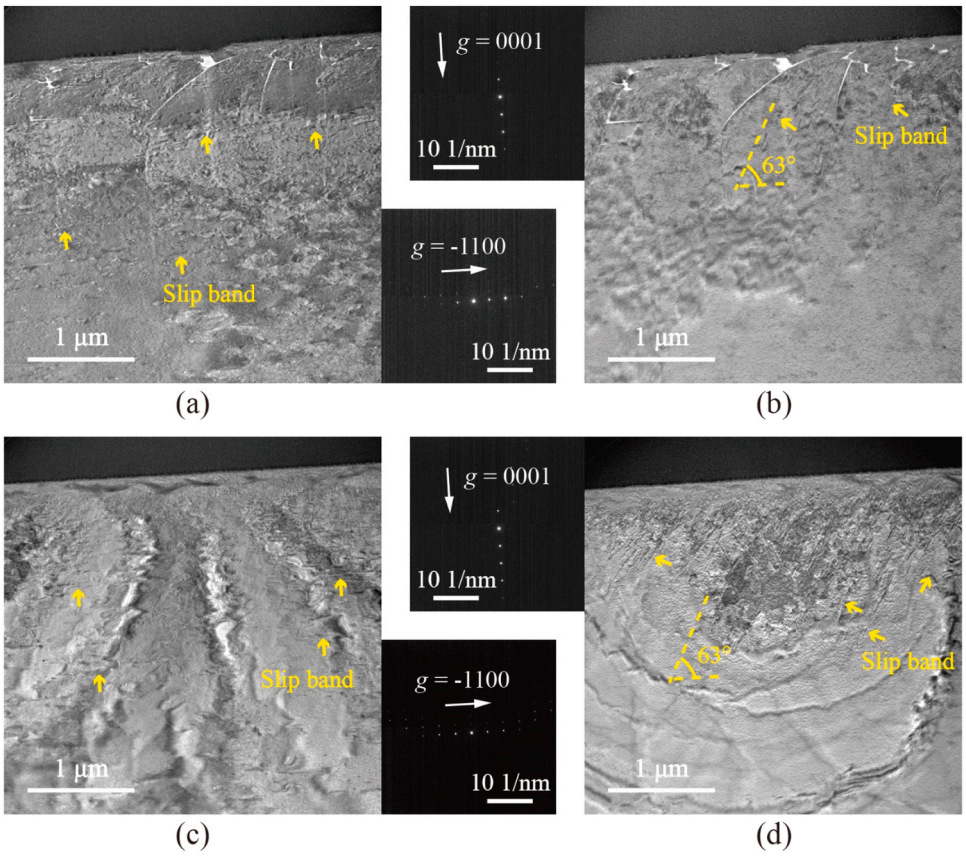

Fig. 12. Cross-sectional TEM images of ZnO subsurface region captured under two-beam conditions: (a, b) CC-processed subsurface with $\boldsymbol{g} = -1100$ and $\boldsymbol{g} = 0001$, respectively; (c, d) UVC-processed subsurface with $\boldsymbol{g} = -1100$ and $\boldsymbol{g} = 0001$, respectively.

The activated slip systems in the CC- and UVC-machined subsurfaces were investigated under two-beam conditions using the $\boldsymbol{g} = 0001$ and $\boldsymbol{g} = -1100$ diffraction vectors, as shown in Fig. 12. For the CC-machined subsurface, slip bands on the (0001) plane, parallel to the surface, were observed under the $\boldsymbol{g} = -1100$ diffraction condition (Fig. 12a) but were invisible under the $\boldsymbol{g} = 0001$ (Fig. 12b). This observation indicates that these slip bands resulted from activation of the basal slip system (0001)<11−20>. Moreover, inclined slip bands on the (−1101) plane, oriented at 63° relative to the surface, were evident under $\boldsymbol{g} = 0001$, indicating that the pyramidal slip system {10−11}<11−23> was also activated. In contrast, for the UVC-machined subsurface, slip bands on the (0001) plane were observed to be more uniformly distributed (Fig. 12c), and inclined slip bands on the (−1101) plane were denser and extended deeper into the subsurface (Fig. 12d). These observations indicate that the cutting process activated both basal and pyramidal slip systems, while ultrasonic vibration assistance further enhanced multi-system slip activity, particularly the pyramidal slip system, thereby significantly enhancing plastic deformation of ZnO crystals.

3.6. Tool wear

After cutting experiments under each condition, the tool edge morphology was examined and compared with that of an unused tool edge to evaluate tool wear behaviour. Fig. 13a shows a SEM image of an unused edge of the diamond tool, which has an intact and sharp edge. In CC under dry conditions, after a cutting distance of approximately 8 m, a wear land with a maximum width (VB) of 3.4 μm was formed, as shown in Fig. 13b. The wear land appeared smooth, indicating stable contact between the tool and the workpiece. In contrast, the tool after UVC under dry conditions (Fig. 13c) exhibited a larger VB of 4.9 μm, characterized by sparse nanoscale grooves aligned with the cutting direction on the wear land, and by deep craters near the boundary between the wear land and the flank face. Additionally, some ZnO chips were found adhered to the worn tool, as confirmed by energy-dispersive X-ray (EDX) elemental analysis in Fig. 13d. This adhesion was likely caused by chips being pressed into the craters and microgrooves on the tool surface during intermittent cutting. Under oil mist lubrication, however, tool wear was suppressed in both CC and UVC. After cutting for 16 m, the wear land resulting from CC exhibited a VB of 1.8 μm as shown in Fig. 13e, whereas the VB from UVC was further reduced to 0.58 μm as shown in Fig. 13f. It is evident that oil mist lubrication plays a key role in reducing tool wear, and tool vibration assistance can further enhance this lubricating effect, thereby reducing tool wear even more.

4. Discussion on cutting and tool wear mechanisms

When using a round-nose tool, the undeformed chip thickness varies along the uncut shoulder, as schematically illustrated in Fig. S7a. A number of studies have demonstrated that during the cutting of brittle materials with a single-crystal diamond tool, the chip formation mode is strongly influenced by the relationship between the undeformed chip thickness (h) and the cutting edge radius (r): when h is much smaller than r, the chip forms via extrusion (Fig. S7b); when h is comparable to r, the chip forms via shearing (Fig. S7c); and when h is much larger than r, the chip forms via fracture (Fig. S7d) [38,48,49]. In this study, the edge radius of the newly manufactured diamond tools was approximately 50 nm, and the maximum undeformed chip thickness under the applied parameters was about 131 nm. During CC with an unworn tool edge, in the region where h was smaller than r (Fig. 14a), a highly negative effective rake angle was induced, causing the material to diverge at the separation point S. Above point S, the material primarily deformed by extrusion, leading to chip formation. Below point S, the material flowed

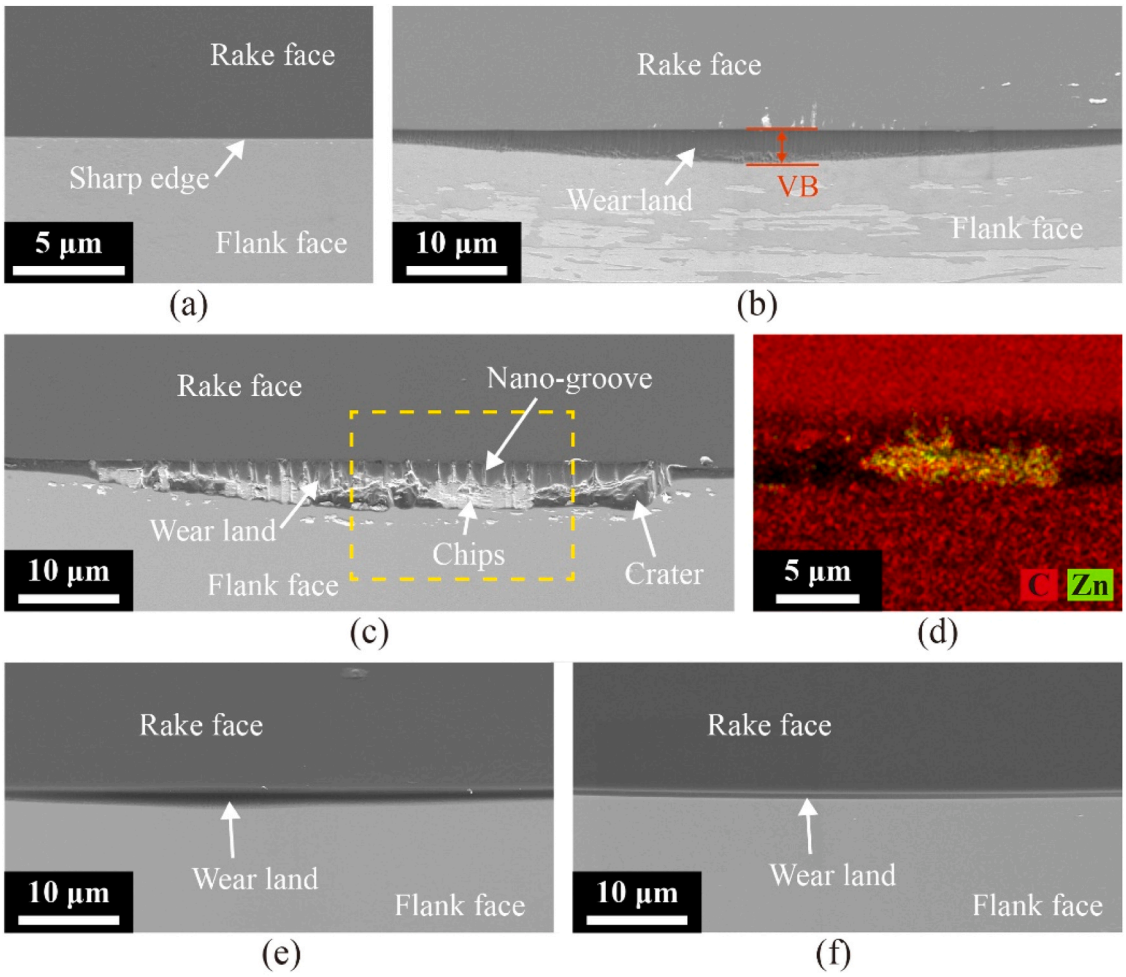

Fig. 13. SEM images of the diamond tool edge: (a) before cutting; after (b) CC and (c) UVC in dry conditions; (d) EDX element mapping analysis within the box in (c); after (e) CC and (f) UVC in oil mist lubrication. (SEM parameters: accelerating voltage of 15.0 kV, and working distance of 9.1 mm.).

downward toward the tool, undergoing plastic and elastic deformation. This ploughing effect caused pits on the machined surface due to tensile stress at the flank face. In contrast, in the region where h was comparable to r, chip formation occurred by shearing, and no brittle fracture took place. Therefore, a transition from extrusion to shearing can be seen in the chip morphology shown in Fig. 6b. During UVC, the tool intermittently engaged with the workpiece at an ultrasonic frequency, traversing an extremely small distance per cycle (theoretically 82 nm), thereby reducing stress concentrations and significantly suppressing the ploughing effect. Meanwhile, the impact induced polycrystallization and promoted pyramidal slip activity, thereby enhancing the surface plasticity. Consequently, even when h was small, chips formed through shear deformation, as illustrated in Fig. 14b.

When tool wear occurred, for CC, the smooth wear land (Fig. 13b) ensured that the effective cutting edge (the intersection of the rake face and wear land) remained sharp. This allowed chip formation to continue through shearing, even though the effective rake angle became less negative. However, the wear land increased friction with the machined surface, generating large tensile stress in the cutting direction, which induced pits on the machined surface, as illustrated in Fig. 14c. For UVC, the nano-grooved wear land (Fig. 13c) led to chipping along the effective cutting edge. Consequently, hydrostatic pressure in front of the cutting edge could not be established, leading to the initiation and propagation of cracks. Due to ZnO's significantly lower stacking fault energy for the basal plane compared to other planes [50], cracks were prone to propagate along the basal plane of the material, resulting in the formation of large craters, as illustrated in Fig. 14d.

It is worth noting that, in dry cutting of ZnO (~4.5 GPa hardness), the tool wear was more significant than that of cutting SiC (~36 GPa hardness) [13]. This implies that, besides mechanical wear, chemical wear plays a dominant role. It is supposed that the wear of diamond tools during cutting ZnO is similar to the CMP of diamond with silica slurry, where C–C bonds on the diamond surface are broken due to the pulling force exerted by the strong C–O bonds formed between the diamond surface and silica particles [51,52]. A schematic of the chemical wear process of the tool during the dry cutting of ZnO is shown in Fig. 14e. As oxygen vacancies (intrinsic defects) are easily generated in ZnO [53], which have also been detected on the machined surface using Raman spectroscopy (Fig. 9), the oxygen atoms in ZnO crystals tend to oxidize the diamond tool during the cutting process by forming C–O bonds. The high-pressure contact between ZnO and diamond under a high local temperature enhances the oxidation of diamond. The friction-induced shear force applied to the flank wear land causes abrasion, progressively removing carbon atoms from the tool surface layer by layer, leading to the rapid growth of the wear land. However, when using the oil mist for lubrication, the tool wear was significantly suppressed. This might be attributed to the oil film sandwiched between the tool and the workpiece, which hindered the oxidation reaction and at the same time reduced the interfacial friction. The tool vibration further enhanced the formation of the oil film, resulting in tool wear suppression.

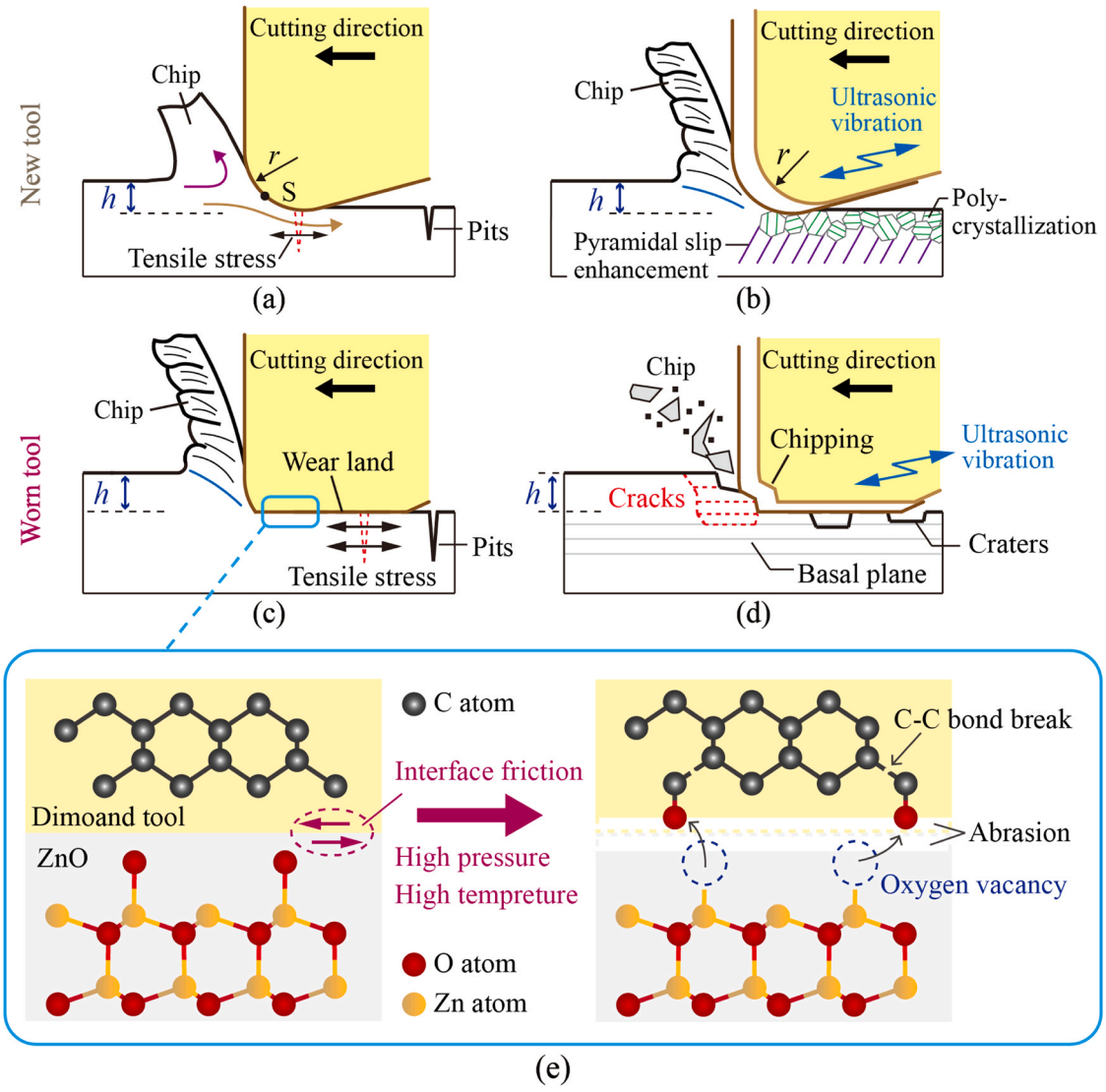

Fig. 14. Schematics of the material removal mechanism during (a) CC and (b) UVC with an unused tool; (c) CC and (d) UVC with a worn tool; (e) the chemical wear process of diamond tools during the cutting of ZnO under dry conditions.

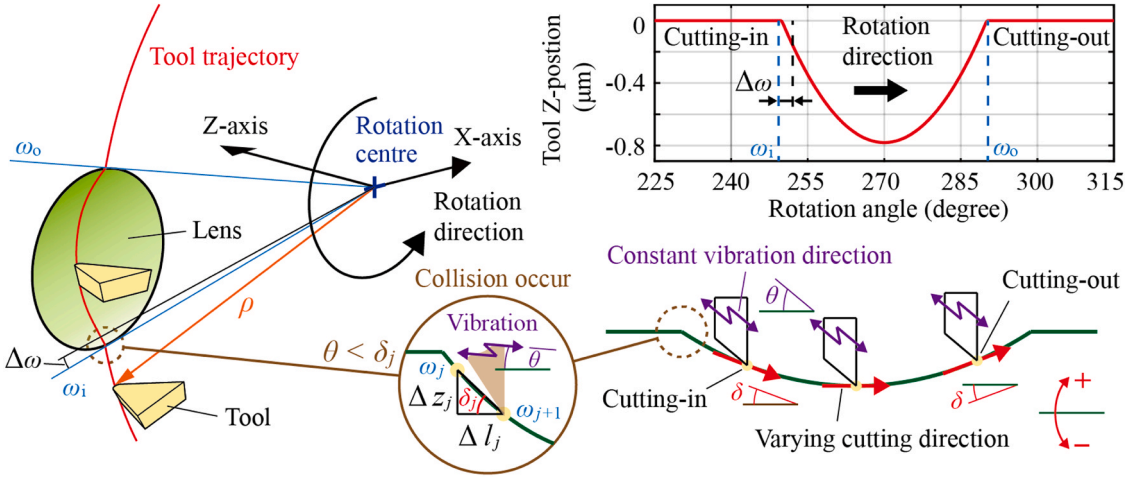

Fig. 15. Schematic illustrating the tool trajectory during lens machining using a slow tool servo, and the direction of ultrasonic vibration of the tool relative to the lens surface.

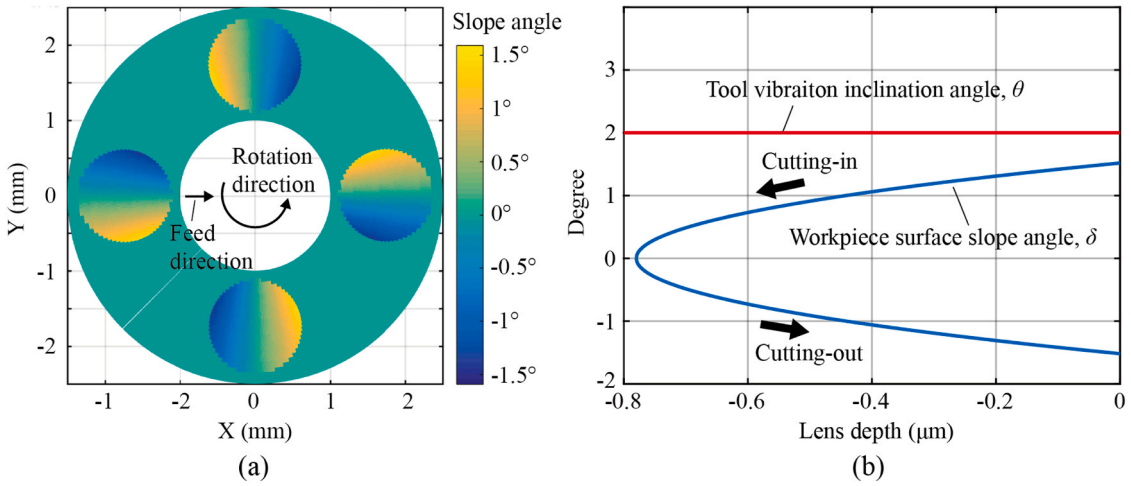

Fig. 16. Illustrations of the microlens surface geometry and the correlation between tool vibration and surface slope: (a) slope angle map of the designed microlens array. (b) relationship between the tool vibration inclination angle and the workpiece surface slope angle at the meridian of a lens.

5. Fabrication of microlens array

Ruling experiments presented in Section 3 have revealed that, although ZnO induces rapid wear on diamond tools, the combined application of ultrasonic vibration assistance and oil mist lubrication during cutting can significantly suppress tool wear, thereby enabling high-quality machined surfaces to be maintained over extended cutting distances. Moreover, under ultrasonic vibration assistance, the distinct difference in machinability between the [11−20] and [1−100] directions disappeared. This is particularly beneficial in turning processes, where the cutting direction continuously changes relative to the crystal orientation. Therefore, during the fabrication of the microlens array using slow tool servo diamond turning, both ultrasonic vibration assistance and oil mist lubrication were applied.

5.1. Geometrical interference analysis

Unlike cutting a flat surface with ultrasonic vibration assistance, machining a curved surface may result in interference between the tool flank and the machined surface during the backward stroke of the vibration cycle. Specifically, the collision of the tool flank with the machined surface will occur if the inclination angle of the tool vibration (θ) is less than the local slope angle of the curved surface (δ). Therefore, when cutting a concave microlens surface, as shown in Fig. 15, such collisions are more likely to occur during the tool's entry into the surface (cutting-in) rather than during its exit from the surface (cutting-out). Since the inclination angle θ is determined by the ultrasonic vibration unit and is constant at 2° in this study, as described in Fig. 2b, it is necessary to examine the global slope angle map of the designed microlens array to determine whether any arbitrary local slope angle δ_j within the concave microlens surface exceeds θ. The local slope angle at an arbitrary point can be expressed as:

$$\delta_j = \arctan\left(\Delta z_j / \Delta l_j\right) \tag{3}$$

$$\Delta z_j = z_{j+1} - z_j \tag{4}$$

$$\Delta l_j = \Delta\omega_j \cdot \rho = \left(\omega_{j+1} - \omega_j\right) \cdot \rho \tag{5}$$

where z_j and z_{j+1} represent the depth coordinates Z of two adjacent points located on a circle of arbitrary radius ρ, coaxial with the rotation centre in the polar coordinate system. Similarly, ω_j and ω_{j+1} denote the rotation angle coordinates C of these two points. Therefore, by substituting the point cloud path data of the designed microlens array, described in the format of (C, ρ, Z), the global slope angle map can be plotted.

Fig. 16a presents the slope angle map of the designed microlens array, where each lens has a diameter of 125 μm and a radius of curvature of 2.5 mm. Along a circular path concentric with the rotation centre, the slope angle gradually decreases from a positive value to a negative value, corresponding to the tool cutting into and then out of the surface. Furthermore, when viewed from the region where the tool first cuts into the surface, the largest slope angle among all concentric circular paths is observed along the path that intersects the deepest point of the lens, also known as the meridian of the lens.

The relationship between local slope angle and lens depth along the

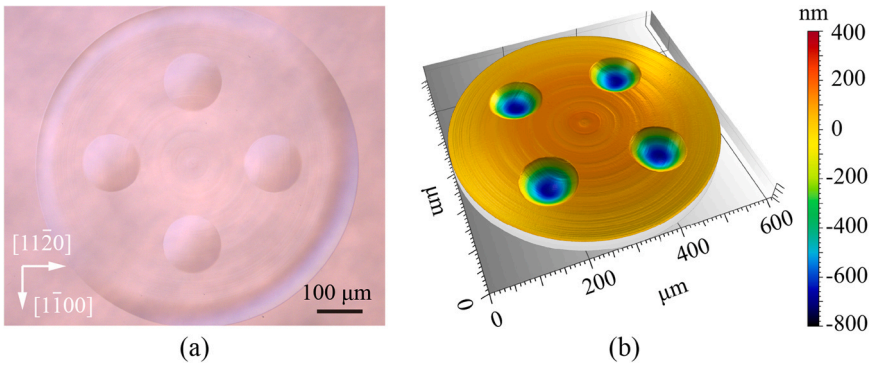

Fig. 17. Machined microlens array using slow tool servo diamond turning combined with ultrasonic vibration assistance under oil mist lubrication conditions: (a) differential interference contrast microscopy image; (b) three-dimensional white light interferometry image.

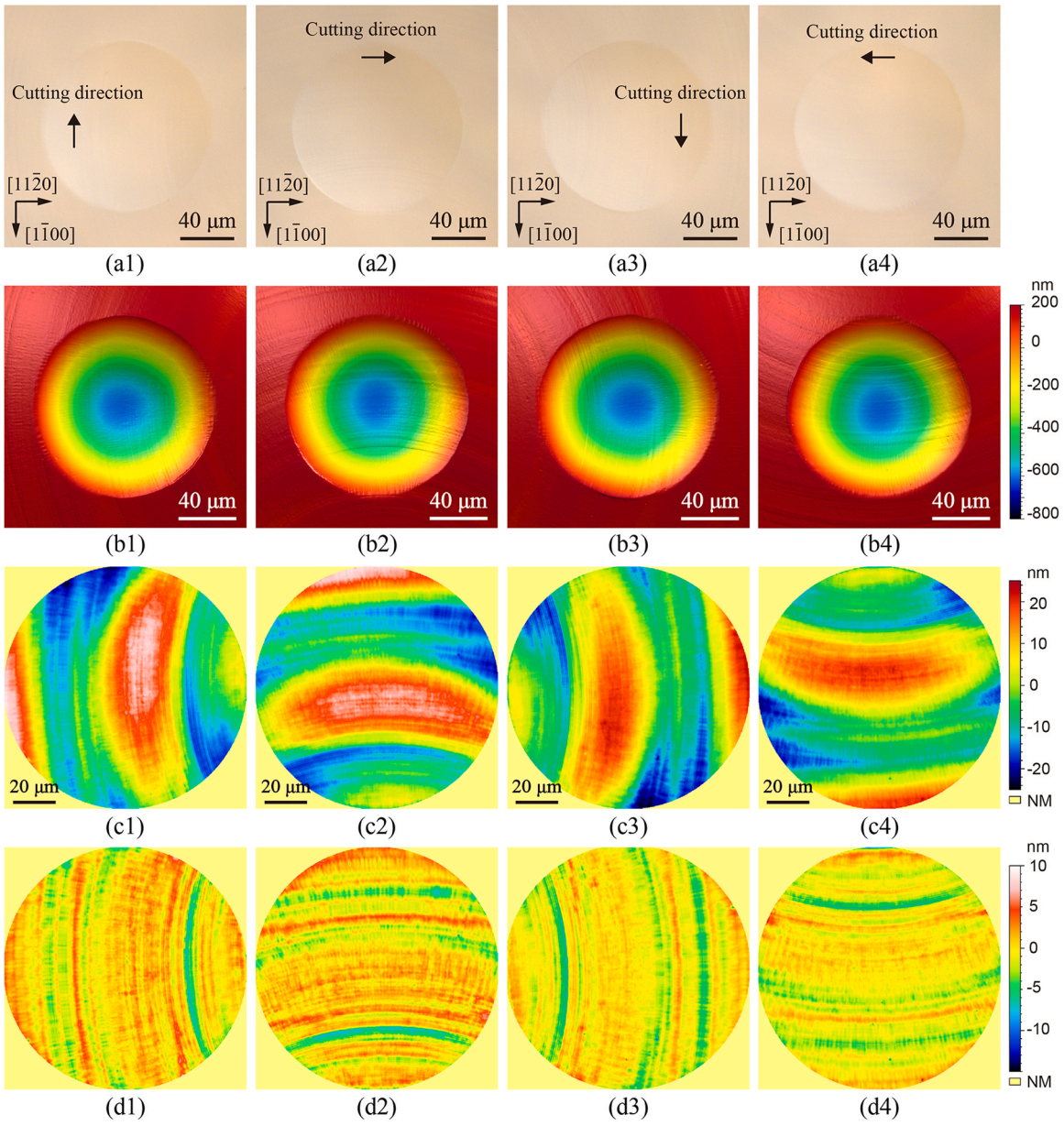

Fig. 18. Detailed views of the four individual microlenses shown in Fig. 17: (a) differential interference contrast microscopy images; (b) three-dimensional white light interferometry images; (c) form error maps by removing a spherical surface having a 2.5 mm radius of curvature from the measured surface shown in (b); (d) surface roughness by applying a Gaussian filter with a cut-off length of 25 μm to the form error maps shown in (c).

meridian of the lens is extracted and shown in Fig. 16b. As the tool cuts into the lens surface, the local slope angle initially reaches a maximum positive value of 1.59° near the edge. The slope angle then gradually decreases, approaching zero at the deepest point. As the tool continues to cut out of the surface, the slope angle becomes negative, mirroring the cutting-in path in both magnitude and shape, thereby resulting in a symmetric distribution. Since the largest local slope angle δ_{max} does not exceed the inclination angle of the tool vibration θ, it is believed that the designed microlens array can be fabricated using the existing ultrasonic vibration unit.

5.2. Lenses topography characterization

Fig. 17a shows a differential interference contrast microscopy image of a diamond-turned circular surface, with four microlenses symmetrically positioned along the circumference. The diagonal lines connecting the microlenses align with the [1−100] and [11−20] directions, respectively. Despite the cutting direction continuously changing relative to the crystal orientation during machining, the diamond-turned flat area exhibited a completely crack-free surface, similar to the initial surface (i.e., the uncut area outside the circular region) prepared by CMP. Moreover, the four microlens areas, where the cutting direction was close to the [1−100] and [11−20] crystallographic directions during machining, also exhibited smooth surfaces. The fracture anisotropy of ZnO was weakened due to the enhanced material plasticity induced by ultrasonic vibration impact (as evidenced by Fig. 12) and the reduced maximum undeformed chip thickness. A three-dimensional white light interferometry image of the diamond-turned circular surface is presented in Fig. 17b. Surface waviness can be observed on the diamond-turned flat area, which may be attributed to unstable temperature conditions that cause the horn of the ultrasonic vibration unit to shrink or expand by several nanometres. Tool wear after microlens array machining was found to be insignificant (Fig. S8).

The detailed views of each microlens were also characterized as

shown in Fig. 18. Differential interference contrast microscopy images (Fig. 18a) revealed that the surfaces of all four microlenses were free of cracks. Fig. 18b presents the three-dimensional white light interferometry images. The depths of the four lenses exhibit excellent consistency, measured at 747 nm ± 1.1 nm. The form error maps shown in Fig. 18c were obtained by subtracting a spherical surface having a 2.5 mm radius of curvature from the measured surface topographies presented in Fig. 18b. The peak-to-valley (PV) form errors of the four microlenses were 47.3, 44.6, 48.4, and 47.6 nm, respectively. After applying a Gaussian filter with a cut-off length of 25 μm to the form error maps shown in Fig. 18c, the surface roughness was obtained and is presented in Fig. 18d. The results indicate that all four lenses exhibited uniformly high surface quality, with root mean square roughness (Sq) values of 1.9, 2.1, 2.2, and 2.0 nm, respectively. The consistently high-quality surfaces of the lenses confirm that the ultrasonic vibration motion did not interfere with the designed surface structure.

6. Conclusions

This study investigated the machining characteristics of ZnO single crystals through ultraprecision diamond cutting using ultrasonic vibration-assisted cutting (UVC) and conventional cutting (CC) under dry and oil mist lubrication conditions. The mechanisms of machined surface formation and tool wear were evidenced by examining the surface topography, subsurface microstructure of the workpiece, chip morphology, cutting forces, and tool morphology. The geometrical interference between the tool and the workpiece during UVC of curved surfaces was discussed, and a high-quality ZnO microlens array was successfully fabricated. Details are summarized as follows:

- Dry cutting (CC and UVC) led to rapid diamond tool wear and surface degradation due to chemical reactions between ZnO oxygen and diamond carbon. Oil mist lubrication significantly reduced wear by forming a protective interfacial film that suppressed chemical reactions.
- Oxygen vacancies were detected on machined surfaces and chips, confirming chemical wear as the dominant tool degradation mechanism. Intermittent cutting in UVC enhanced oil film formation, which further mitigated tool wear.
- In the CC of ZnO, anisotropic machinability was observed, with cutting along the [11−20] direction producing better surface quality than the [1−100] direction. This may be attributed to the slightly higher atomic packing density and bond strength on the (11−20) plane compared to the (1−100) plane.
- In the ZnO subsurface machined by CC and UVC, a high density of dislocations was formed near the surface, accompanied by the activation of both basal and pyramidal slip systems. UVC further induced polycrystallization near the surface and enhanced pyramidal slip activity in the subsurface region, thereby promoting plastic deformation of the material. As a result, UVC mitigated the anisotropic nature of material removal and achieved better surface quality compared to CC.
- During UVC of curved surfaces, the inclination angle of the tool vibration should exceed the maximum slope angle of the curved surface to prevent collision with the machined surface. A high-quality microlens array was fabricated on ZnO using slow tool servo diamond turning with ultrasonic vibration assistance under oil mist lubrication, achieving a surface roughness below 2.2 nm Sq and a form error below 49 nm peak-to-valley.

This research provides evidence that UVC combined with oil mist lubrication represents an optimal approach for ultraprecision diamond cutting of ZnO, in terms of both tool wear reduction and enhancement of material plasticity. The feasibility of using the cutting method to fabricate micro-structured surfaces on ZnO was validated through the integration of slow tool servo diamond turning and UVC under oil mist lubrication. This approach may also serve as a valuable reference for optimizing machining conditions not only for ZnO but also for other brittle oxide crystals commonly used in the optical manufacturing industry.

CRediT authorship contribution statement

Weihai Huang: Writing – original draft, Visualization, Validation, Methodology, Investigation, Data curation, Conceptualization. **Takeshi Hashimoto:** Software, Validation, Methodology, Data curation. **Jiwang Yan:** Writing – review & editing, Supervision, Resources, Project administration, Methodology, Funding acquisition, Conceptualization.

Declaration of Competing Interest

The authors declare that they have no known competing financial interests or personal relationships that could have appeared to influence the work reported in this paper.

Acknowledgement

This work has been partially supported by Japan Society for the Promotion of Science under the Grant-in-Aid for JSPS Fellows, project number 24KF0255, and the Grant-in-Aid for Scientific Research (A), project number 25H00709.

Appendix A. Supporting information

Supplementary data associated with this article can be found in the online version at doi:10.1016/j.jmatprotec.2025.119026.

References

[1] Xu, W.Z., Ye, Z.Z., Zeng, Y.J., Zhu, L.P., Zhao, B.H., Jiang, L., Lu, J.G., He, H.P., Zhang, S.B., 2006. ZnO light-emitting diode grown by plasma-assisted metal organic chemical vapor deposition. Appl. Phys. Lett. 88 (17), 173506.
[2] Özgür, Ü., Hofstetter, D., Morkoç, H., 2010. ZnO devices and applications: a review of current status and future prospects. Proc. IEEE 98 (7), 1255–1268.
[3] Panda, S.K., Jacob, C., 2012. Preparation of transparent ZnO thin films and their application in UV sensor devices. SolidState Electron. 73, 44–50.
[4] Avrutin, V., Cantwell, G., Zhang, J., Song, J.J., Silversmith, D.J., Morkoç, H., 2010. Bulk ZnO: current status, challenges, and prospects. Proc. IEEE 98 (7), 1339–1350.
[5] Lucca, D.A., Hamby, D.W., Klopfstein, M.J., Cantwell, G., Wetteland, C.J., Teşmer, J.R., Nastasi, M., 2001. Effects of polishing on the photoluminescence of single crystal ZnO. CIRP Ann. 50 (1), 397–400.
[6] Li, H., Li, T., Chen, S., Wu, Y., 2023. Photoelectric hybrid neural network based on ZnO nematic liquid crystal microlens array for hyperspectral imaging. Opt. Express 31 (5), 7643–7658.
[7] Fei, C., Hsu, H., Vafanejad, A., Li, Y., Lin, P., Li, D., Yang, Y., Kim, E., Shung, K.K., Zhou, Q., 2017. Ultrahigh frequency ZnO silicon lens ultrasonic transducer for cell-size microparticle manipulation. J. Alloy. Compd. 729, 556–562.
[8] Brinksmeier, E., Karpuschewski, B., Yan, J., Schönemann, L., 2020. Manufacturing of multiscale structured surfaces. CIRP Ann. 69 (2), 717–739.
[9] Zong, W.J., Cao, Z.M., He, C.L., Xue, C.X., 2016. Theoretical modelling and FE simulation on the oblique diamond turning of ZnS crystal. Int. J. Mach. Tools Manuf. 100, 55–71.
[10] Huang, W., Yan, J., 2020. Surface formation mechanism in ultraprecision diamond turning of coarse-grained polycrystalline ZnSe. Int. J. Mach. Tools Manuf. 153, 103554.
[11] Huang, W., Yan, J., 2023. Effect of tool geometry on ultraprecision machining of soft-brittle materials: a comprehensive review. Int. J. Extrem. Manuf. 5 (1), 012003.
[12] Li, C., Wang, K., Piao, Y., Cui, H., Zakharov, O., Duan, Z., Zhang, F., Yan, Y., Geng, Y., 2024. Surface micro-morphology model involved in grinding of GaN crystals driven by strain-rate and abrasive coupling effects. Int. J. Mach. Tools Manuf. 201, 104197.
[13] Huang, W., Yan, J., 2023. Mechanisms of tool-workpiece interaction in ultraprecision diamond turning of single-crystal SiC for curved microstructures. Int. J. Mach. Tools Manuf. 191, 104063.
[14] Zou, L., Yin, J., Huang, Y., Zhou, M., 2018. Essential causes for tool wear of single crystal diamond in ultra-precision cutting of ferrous metals. Diam. Relat. Mater. 86, 29–40.
[15] Yang, Z., Zhu, L., Zhang, G., Ni, C., Lin, B., 2020. Review of ultrasonic vibration-assisted machining in advanced materials. Int. J. Mach. Tools Manuf. 156, 103594.
[16] Moriwaki, T., Shamoto, E., 1991. Ultraprecision diamond turning of stainless steel by applying ultrasonic vibration. CIRP Ann. 40 (1), 559–562.

[17] Shamoto, E., Moriwaki, T., 1994. Study on elliptical vibration cutting. CIRP Ann. 43 (1), 35–38.
[18] Nath, C., Rahman, M., Neo, K.S., 2011. Modeling of the effect of machining parameters on maximum thickness of cut in ultrasonic elliptical vibration cutting. J. Manuf. Sci. Eng. 133 (1), 011007.
[19] Huang, W., Yu, D., Zhang, X., Zhang, M., Chen, D., 2018. Ductile-regime machining model for ultrasonic elliptical vibration cutting of brittle materials. J. Manuf. Process. 36, 68–76.
[20] Wang, J., Liao, W., Guo, P., 2020. Modulated ultrasonic elliptical vibration cutting for ductile-regime texturing of brittle materials with 2-D combined resonant and non-resonant vibrations. Int. J. Mech. Sci. 170, 105347.
[21] Zhang, J., Suzuki, N., Wang, Y., Shamoto, E., 2014. Fundamental investigation of ultra-precision ductile machining of tungsten carbide by applying elliptical vibration cutting with single crystal diamond. J. Mater. Process. Technol. 214 (11), 2644–2659.
[22] Gaidys, R., Dambon, O., Ostasevicius, V., Dicke, C., Narijauskaite, B., 2017. Ultrasonic tooling system design and development for single point diamond turning (SPDT) of ferrous metals. Int. J. Adv. Manuf. Technol. 93 (5), 2841–2854.
[23] Zhang, C., Cheung, C., Bulla, B., Zhao, C., 2021. An investigation of the high-frequency ultrasonic vibration-assisted cutting of steel optical moulds. Micromachines 12 (4), 460.
[24] Guo, J., Zhang, J., Pan, Y., Kang, R., Namba, Y., Shore, P., Yue, X., Wang, B., Guo, D., 2020. A critical review on the chemical wear and wear suppression of diamond tools in diamond cutting of ferrous metals. Int. J. Extrem. Manuf. 2 (1), 012001.
[25] Pan, Y., Kang, R., Bao, Y., Yin, S., Dong, Z., 2023. Study on tool wear mechanism of single-crystal diamond in ultrasonic vibration elliptical cutting of tungsten heavy alloy. Wear, 204616, 516-517.
[26] Liang, X., Zhang, C., Cheung, C.F., Wang, C., Li, K., Bulla, B., 2023. Micro/nano incremental material removal mechanisms in high-frequency ultrasonic vibration-assisted cutting of 316L stainless steel. Int. J. Mach. Tools Manuf. 191, 104064, 38.
[27] Chen, Y., Sun, L., Chen, M., Wu, Y., 2023. Reducing the cutting tool wear in diamond turning of zerodur glass-ceramic by the mechanical cleaning effect of ultrasonic vibration assistance. J. Manuf. Process. 104, 460–471.
[28] Zhang, J., Zheng, Z., Huang, K., Lin, C., Huang, W., Chen, X., Xiao, J., Xu, J., 2024. Field-assisted machining of difficult-to-machine materials. Int. J. Extrem. Manuf. 6 (3), 032002.
[29] Zheng, Z., Huang, K., Lin, C., Huang, W., Zhang, J., Chen, X., Xiao, J., Xu, J., 2023. Analytical modeling of subsurface damage and material removal energy in elliptical vibration cutting of micro-structures on brittle materials. J. Mater. Res. Technol. 25, 5674–5692.
[30] Wang, Y., Liang, Z., Zhao, W., Wang, X., Wang, H., 2020. Effect of ultrasonic elliptical vibration assistance on the surface layer defect of M-plane sapphire in microcutting. Mater. Des. 192, 108755.
[31] Huang, W., Yan, J., 2023. Towards understanding the mechanism of vibration-assisted cutting of monocrystalline silicon by cyclic nanoindentation. J. Mater. Process. Technol. 311, 117797.
[32] Zheng, Z., Huang, K., Lin, C., Huang, W., Zhang, J., Chen, X., Xiao, J., Xu, J., 2023. Analytical modeling of subsurface damage and material removal energy in elliptical vibration cutting of micro-structures on brittle materials. J. Mater. Res. Technol. 25, 5674–5692.
[33] Yin, S., Yip, W.S., Dong, Z., Kang, R., To, S., 2025. Experimental and simulation investigation of ultrasonic elliptical vibration cutting of tungsten alloys in ultra-precision machining. J. Mater. Res. Technol. 34, 77–89.
[34] Zhao, L., Zhang, J., Zhang, J., Hartmaier, A., 2021. Atomistic investigation of machinability of monocrystalline 3C–SiC in elliptical vibration-assisted diamond cutting. Ceram. Int. 47 (2), 2358–2366.
[35] Lucca, D.A., Klopfstein, M.J., Ghisleni, R., Cantwell, G., 2002. Investigation of polished single crystal ZnO by nanoindentation. CIRP Ann. 51 (1), 483–486.
[36] Gao, C., Liu, G., Yang, R., Zakharov, O., Geng, Y., Li, C., 2025. Understanding crack initiation and propagation mechanisms of ZnO crystals induced by nanoindentation and nanoscratch. Mater. Today Commun. 45, 112425.
[37] Huang, W., Yan, J., 2025. Revealing the mechanism of crystal orientation-dependent surface morphology and topography evolution in single-crystal ZnO using nanoindentation. Mater. Des. 257, 114531.
[38] Blackley, W.S., Scattergood, R.O., 1991. Ductile-regime machining model for diamond turning of brittle materials. Precis. Eng. 13 (2), 95–103.
[39] ISO 21920-3:2021 Geometrical product specifications (GPS) — Surface texture: Profile. Part 3: Specification operators.
[40] Xing, Y., Liu, Y., Yin, T., Li, D., Sun, Z., Xue, C., Yip, W.S., To, S., 2024. Magnetic and ultrasonic vibration dual-field assisted ultra-precision diamond cutting of high-entropy alloys. Int. J. Mach. Tools Manuf. 202, 104208.
[41] Liu, K., Li, X.P., Rahman, M., Neo, K.S., Liu, X.D., 2006. A study of the effect of tool cutting edge radius on ductile cutting of silicon wafers. Int. J. Adv. Manuf. Technol. 32 (7), 631–637.
[42] Šćepanović, M., Grujić-Brojčin, M., Vojisavljević, K., Bernik, S., Srećković, T., 2010. Raman study of structural disorder in ZnO nanopowders. J. Raman Spectrosc. 41 (9), 914–921.
[43] Alarcón-Lladó, E., Ibáñez, J., Artús, L., Jiménez, J., Wang, B., Callahan, M.J., Cuscó, R., 2007. Temperature dependence of Raman scattering in ZnO. Phys. Rev. B 75 (16), 165202.
[44] Silva, R.L.D.S., Franco Jr, A., 2020. Raman spectroscopy study of structural disorder degree of ZnO ceramics. Mater. Sci. Semicond. Process. 119, 105227.
[45] Tripathi, N., Vijayarangamuthu, K., Rath, S., 2011. A Raman spectroscopic study of structural evolution of electrochemically deposited ZnO films with deposition time. Mater. Chem. Phys. 126 (3), 568–572.
[46] Decremps, F., Pellicer-Porres, J., Saitta, A.M., Chervin, J., Polian, A., 2002. High-pressure Raman spectroscopy study of wurtzite ZnO. Phys. Rev. B 65 (9), 092101.
[47] He, Y., Zou, P., Zhu, W., Ehmann, K.F., 2017. Ultrasonic elliptical vibration cutting of hard materials: simulation and experimental study. Int. J. Adv. Manuf. Technol. 91 (1), 363–374.
[48] Yan, J., Syoji, K., Kuriyagawa, T., 1999. Chip morphology of ultra-precision diamond turning of single crystal silicon. J. Jpn. Soc. Precis. Eng. 65 (7), 1008–1012.
[49] Fang, F.Z., Wu, H., Zhou, W., Hu, X.T., 2007. A study on mechanism of nano-cutting single crystal silicon. J. Mater. Process. Technol. 184 (1), 407–410.
[50] Yan, Y., Dalpian, G.M., Al-Jassim, M.M., Wei, S., 2004. Energetics and electronic structure of stacking faults in ZnO. Phys. Rev. B 70 (19), 193206.
[51] Peguiron, A., Moras, G., Walter, M., Uetsuka, H., Pastewka, L., Moseler, M., 2016. Activation and mechanochemical breaking of C–C bonds initiate wear of diamond (110) surfaces in contact with silica. Carbon 98, 474–483.
[52] Thomas, E.L.H., Nelson, G.W., Mandal, S., Foord, J.S., Williams, O.A., 2014. Chemical mechanical polishing of thin film diamond. Carbon 68, 473–479.
[53] Fukushima, H., Uchida, H., Funakubo, H., Katoda, T., Nishida, K., 2017. Evaluation of oxygen vacancies in ZnO single crystals and powders by micro-Raman spectroscopy. J. Ceram. Soc. Jpn. 125 (6), 445–448.